Asymmetric Particle Aggregation in Ocean Eddies Driven by Eddy-Wind Interactions

Qinbiao Ni[1], Xiaoming Zhai[2], and Dake Chen[1,3]

[1]Southern Marine Science and Engineering Guangdong Laboratory (Zhuhai), Zhuhai, China

[2]Centre for Ocean and Atmospheric Sciences, School of Environmental Sciences, University of East Anglia, Norwich, UK

[3]State Key Laboratory of Satellite Ocean Environment Dynamics, Second Institute of Oceanography, Ministry of Natural Resources, Hangzhou, China

Corresponding author: Qinbiao Ni (niqinbiao@outlook.com)

Key Points

- Cyclonic eddies globally trap ~12.5% more drifters than anticyclonic eddies
- The asymmetry in drifter clustering is most prominent near the eddy centers
- Ekman pumping during eddy-wind interactions leads to the asymmetry

Abstract

Mesoscale eddies, prevalent across the global ocean, play a crucial role in the transport and mixing of climate-sensitive tracers such as heat, salt, and nutrients. While traditional quasi-geostrophic theory predicts symmetric kinematics and equivalent material transport by cyclonic and anticyclonic eddies, our analysis of satellite altimeter and surface drifter data shows a significant asymmetry in drifter distribution inside ocean eddies. We find that globally cyclonic eddies capture about 12.5% more drifters than their anticyclonic counterparts, particularly near eddy centers. Numerical experiments reveal that this asymmetry results from eddy-wind interactions, which induce anomalous convergence in cyclonic eddies and divergence in anticyclonic eddies, enhancing particle aggregation in cyclones. These findings provide new insights into the distribution of ocean surface buoyant materials, including oil spills, plastics, and other pollutants.

Plain language summary

Swirling water motions, known as mesoscale eddies, are common phenomena of the ocean. Scientists have long assumed that the two types of these eddies, cyclonic versus anticyclonic, transport materials in the same way. However, by analyzing data from satellites that measure sea surface height and floating devices that track surface water movement, we show a clear difference in how small particles accumulate in these two eddy types across the world's oceans. Computer simulations further reveal that interactions between the eddies and winds are the main reason for this difference. Our results offer new perspectives on how oceanic eddies spread light materials near the sea surface and highlight the need to include this process into climate models for more accurate climate predictions.

1. Introduction

Satellite observations have unveiled a highly turbulent ocean surface, populated by mesoscale cyclonic (CEs) and anticyclonic eddies (AEs) with spatial scales ranging from tens to hundreds of kilometers (Chelton et al., 2007; 2011; Ni et al., 2020). These eddies, primarily generated from instabilities of the general ocean circulation (Gill et al., 1974; Ferrari and Wunsch, 2009; Zhai and Marshall, 2013), play a critical role in shaping large-scale gyres, modulating air-sea exchanges, and redistributing oceanic

properties including mass, carbon, and pollutants (Qiu and Chen, 2005; Jing et al., 2020; Frenger et al., 2013; Gaube et al., 2015; Zhang et al., 2014; Gruber et al., 2011).

Classical quasi-geostrophic theory predicts perfect symmetry in the structure and kinematics of CEs and AEs (McWilliams, 2008), implying equivalent material trapping capabilities for the two eddy types. This equal trapping assumption is widely accepted in eddy transport research, though the exact magnitude of eddy trapping efficiency remains debated (Zhang et al., 2014; Dong et al., 2014; Sun et al., 2019; Abernathey and Haller, 2018; Liu et al., 2022; Xia et al., 2022). However, Vic et al. (2022) found that CEs contain more surface drifters than AEs in the North Atlantic, challenging the common assumption. It remains unclear whether this eddy clustering asymmetry exists globally. Moreover, the spatial pattern of material aggregation inside eddies is poorly understood: does enhanced drifter clustering occur at CE centers or edges? Resolving this spatial distribution may provide important insights into physical mechanisms driving the eddy trapping asymmetry.

Two candidate processes may explain why CEs cluster more surface drifters than AEs. The first is ageostrophic frontogenesis, which is thought to induce material convergence in cyclonic regions during CE formation (Vic et al., 2022). This effect is expected to be strongest at eddy edges where frontogenesis is most active (Capet et al., 2008; Siegel et al., 2011; Zhang et al., 2018). The second is eddy-wind interactions. The relative wind effect, accounting for the relative motion between surface winds and ocean currents, induces Ekman divergence in AEs and Ekman convergence in CEs (Stern, 1965). This favors material aggregation at CE centers where Ekman pumping peaks (McGillicuddy et al., 2007; Gaube et al., 2015; Wilder et al., 2022). In this study, we use global observations to document this eddy clustering asymmetry and conduct numerical experiments to identify its driving mechanisms.

2. Data and methods

2.1. Data processing

Daily 1/4° altimeter sea level anomaly (SLA) data are sourced from the Copernicus Marine Environment Monitoring Service. To remove large-scale signals, we apply a high-pass spatial Gaussian filter with a half-power cutoff wavelength of 20° to each SLA map (Ni et al., 2023a). Six-hourly trajectory and velocity data from

drogued surface drifters are provided by the Global Drifter Program. Hourly MERRA-2 wind vector data (0.5° latitude × 0.625° longitude) are obtained from the NASA Global Modeling and Assimilation Office, while hourly 1/4° ERA5 wind vector data are provided by the European Centre for Medium-Range Weather Forecasts. Daily mid-time winds are low-pass-filtered with the same 20° cutoff wavelength to extract large-scale background winds. Argo float trajectory data come from the China Argo Real-time Data Center. All datasets spanning 1998-2017 are used in this study.

2.2. Eddy detection and compositing

Mesoscale eddies are identified from the high-pass-filtered SLA data using a geometry-based eddy detection algorithm (Chelton et al., 2011; Ni et al., 2020). SLA contours are extracted at 1-cm intervals. Eddy center is the average of the innermost closed contour, and eddy edge is the outermost closed contour containing no more than one eddy center. Eddy radius equals the radius of a circle matching the area bounded by the eddy edge. Small-size mesoscale eddies at high latitudes are excluded in this study due to limited resolution of current SLA data. For composite analysis, we establish a 0.1r×0.1r grid (r is the eddy radius; Chaigneau et al., 2011; Ni et al., 2021), centered on each eddy center with positive x-axis eastward and positive y-axis northward. Surface drifter trajectories and velocities are projected onto this normalized eddy-centric coordinate system (Fig. S1) for compositing.

2.3. Ekman transport and pumping

The anomalous Ekman transport (Price et al., 2008) is calculated from

$$\boldsymbol{T} = \frac{\boldsymbol{\tau_{rel}} - \boldsymbol{\tau_{abs}}}{\rho f}, \quad (1)$$

where ρ is the seawater density, f is the Coriolis parameter, $\boldsymbol{\tau_{rel}} = \rho_a c_d (\boldsymbol{u}_w - \boldsymbol{u}_o)|\boldsymbol{u}_w - \boldsymbol{u}_o|$ is the relative wind stress, and $\boldsymbol{\tau_{abs}} = \rho_a c_d (\boldsymbol{u}_w)|\boldsymbol{u}_w|$ is the absolute wind stress (where ρ_a is the air density, c_d is the drag coefficient, $\boldsymbol{u}_w$ is the surface 10-m wind velocity, and $\boldsymbol{u}_o$ is the surface ocean current velocity). Relative wind stress accounts for the relative motion between surface winds and ocean surface currents, which induces Ekman pumping velocities inside mesoscale eddies. In contrast, absolute wind stress depends on surface winds alone and produces no such vertical velocities.

Ekman pumping is calculated as follows (Stern, 1965; McGillicuddy et al., 2007;

Gaube et al., 2015):

$$w = \frac{1}{\rho}\nabla \times \left(\frac{\boldsymbol{\tau_{rel}}}{f+\xi}\right) \approx \frac{\nabla \times \boldsymbol{\tau_{rel}}}{\rho(f+\xi)} + \frac{\boldsymbol{\tau_{rel}} \cdot \nabla \xi}{\rho(f+\xi)^2}, \quad (2)$$

where $\xi = \frac{\partial v_o}{\partial x} - \frac{\partial u_o}{\partial y}$ is the relative vorticity of ocean surface geostrophic currents. Equation 2 contains two dynamical terms. The first term relates directly to wind stress curl, producing a monopolar vertical velocity pattern centered at the eddy core insensitive to wind direction. The second term arises from the interaction between the wind stress and relative vorticity gradient, yielding a wind-direction-dependent dipolar vertical velocity structure. Eddy-induced sea surface temperature anomalies can also generate dipolar vertical velocities (Gaube et al., 2015). When integrated over the eddy area, these dipolar signals are largely canceled out. We therefore only consider the first term in the subsequent analysis.

2.4. Initial eddy field

Three-dimensional eddy temperature and salinity fields used for our modeling study are initialized by

$$F = E'_h \cdot E'_v + \bar{F}, \quad (3)$$

where E'_h is the horizontal structure of random eddies synthesized by superposing sinusoidal functions (Brannigan et al., 2015):

$$E'_h = [\sum_{k,l=1}^{20} \sin\left(\frac{2\pi kx}{L} + \theta_1(k,l)\right) \cdot \sin\left(\frac{2\pi ly}{L} + \theta_2(k,l)\right) \cdot G_n(\boldsymbol{k})], \quad (4)$$

where k and l are the zonal and meridional components of the wavenumber vector $\boldsymbol{k}$, L is the domain size, θ_i is random phase angle, and $G_n(\boldsymbol{k}) = e^{-\frac{1}{2}\left(\frac{\boldsymbol{k}-k_0}{3.5}\right)^2}$ is a Gaussian function confining the eddy length scale around $\boldsymbol{k} = k_0$. Square brackets represent normalization by the eddy-centric mean. The vertical eddy temperature or salinity profile E'_v comes from Argo composite analysis, and the climatological profile $\bar{F}$ is obtained from World Ocean Atlas 2018 data. These profiles match Figure 3 in Ni et al. (2023b). Initial density uses MITgcm's linear equation of state (eosType='LINEAR'), and horizontal velocities are calculated via the thermal wind balance.

2.5. Numerical experiments

To investigate the mechanism behind the observed drifter clustering asymmetry

between CEs and AEs, we perform two sets of idealized numerical experiments using the MITgcm (Marshall et al., 1997). The model runs on an f-plane at 30°N latitude with double periodic boundary conditions. The rectangular domain extends 1000 km in both horizontal directions and reaches 4000-m depth. The mean initial eddy radius is 80 km, corresponding to k_0 = 1000 km / (4×80 km) = 3.1 in Equation 4. Horizontal resolution is set to 10 km, insufficient to resolve submesoscale motions. There are 60 levels in the vertical, ranging from 2 m near the surface to 200 m near the seafloor. Horizontal mixing employs a Laplacian operator (5 m^2 s^{-1}), while vertical mixing adopts the K-profile parameterization scheme (Large et al., 1994), with a background diffusivity of 10^{-5} m^2 s^{-1}.

The two sets of numerical experiments differ only in wind stress forcing: Experiment 1 uses absolute wind stress, while Experiment 2 uses relative wind stress. A spatially uniform eastward wind of 13 m s^{-1} is applied over the eddy field. To mimic surface drifters, Lagrangian particles are released at ~15-m depth from every-other grid point at simulation onset via MITgcm's FLT package. Their trajectories are recorded at 6-hour intervals. Each experiment comprises an ensemble of 10 simulations, initialized with random eddy fields reconstructed from Equation 3.

3. Results

3.1. Drifter aggregation inside eddies

To investigate material clustering by mesoscale eddies, we combine three global datasets: satellite altimeters, surface drifters and MERRA-2 winds from 1998 to 2017. Eddies are detected from daily SLA fields (Fig. S1), using a well-established SLA-contour method (Chelton et al., 2011; Ni et al., 2020). Then, an eddy-centric coordinate system is set up for each eddy (Chaigneau et al., 2011; Ni et al., 2021). Surface drifter data are further projected onto this coordinate system for composite analysis. Full technical details are given in the Methods section. Globally over 20 years, 14.8 million snapshots of CEs, with a mean radius of 79.8±39.4 km, and 14.4 million snapshots of AEs, with a mean radius of 80.6±39.9 km, are identified. There are 3.6 million drifter records inside CEs versus 3.2 million inside AEs. With nearly equal total surface area, CEs contain 12.5% more drifters than AEs on a global scale.

To characterize the global distribution of eddy clustering asymmetry, we calculate

the relative difference in drifter records between CEs and AEs in 5°×5° bins using metric $\gamma = (N_{CEs} - N_{AEs})/N_{AEs}$, where N_{CEs} and N_{AEs} represent the drifter record numbers within one eddy radius of CEs and AEs, respectively. The γ is significantly larger in strong current regions and at low latitudes (Fig. 1a), where eddy-induced Ekman pumping is strongest (Figs. 1b-c; Gaube et al., 2015). Negative values emerge in some regions (e.g., the northeastern Pacific), indicating locally greater drifter aggregation in AEs. We suspect that this discrepancy arises because the initial metric ignores regionally variable eddy areal coverage. We therefore refine the metric to $\gamma_S = (N_{CEs}/S_{CEs} - N_{AEs}/S_{AEs})/(N_{AEs}/S_{AEs})$, where S_{CEs} and S_{AEs} denote the total CE and AE areas per bin. The resulting γ_S values are mostly positive (Fig. 1d), confirming that CEs generally trap more drifters than AEs after eddy area normalization.

Composite analysis of surface drifter records in the eddy-centric coordinate system also reveals a significant difference between CEs and AEs in both hemispheres. Using a 0.1r × 0.1r eddy grid, the number of drifter records at CE center (~7900) is 40% higher than that at AE center (~5600), with both eddy types containing more drifters than ambient waters (Figs. 2a-d). This provides the first global observational evidence that CEs cluster more surface particles than AEs, consistent with the North Atlantic results (Vic et al., 2022) and challenging the long-standing kinematic symmetry assumption (McWilliams, 2008; Zhang et al., 2014; Liu et al., 2022). In addition, AEs exhibit relatively uniform drifter distribution, while CEs' drifter concentrations increase gradually from edge to center (Figs. 2a-d). This pattern supports eddy-wind interactions as the dominant mechanism, rather than periphery-dominated frontogenesis (Capet et al., 2008; Siegel et al., 2011; Zhang and Qiu, 2018).

3.2. Relationship with Ekman pumping

When background winds blow over mesoscale eddies, the relative wind stress is weaker on the side where winds and currents align and stronger on the side where they oppose. This relative wind stress variation generates Ekman convergence over CEs and divergence over AEs, triggering downwelling within cyclones and upwelling within anticyclones. We next explore how eddy-wind interactions produce the observed eddy clustering asymmetry. Using global daily MERRA-2 winds and altimeter-derived geostrophic currents, both interpolated to drifter locations, we calculate the anomalous Ekman transport and Ekman pumping induced by the relative wind effect (see

Methods). Consistent with previous studies (McGillicuddy et al., 2007; Gaube et al., 2015), the relative wind stress drives Ekman convergence and downwelling inside CEs and Ekman divergence and upwelling inside AEs (Figs. 2e-h). Eddy-centric mean Ekman pumping velocities reach ~15 cm day^{-1}, regardless of hemisphere or eddy polarity. Replacing MERRA-2 with ERA5 wind data yields similar results (Fig. S2).

If eddy-wind interactions are responsible for the observed eddy trapping asymmetry, we would expect this asymmetry to intensify with increasing Ekman pumping. To test this hypothesis, we compare drifter aggregation in CEs and AEs against the Ekman pumping velocities at the eddy centers. The Ekman pumping velocity at the center of each eddy is diagnosed (see Methods) and categorized into groups by magnitude. Drifter record counts within and around eddies are composited per group in the eddy-centric coordinate system. For weak Ekman pumping, drifter distributions are uniform and comparable between CEs and AEs (Figs. 3a-d). As Ekman pumping increases, the clustering asymmetry grows, with greater drifter accumulation in CE core (Figs. 3e-l). We quantify this disparity via the relative difference (i.e., $\gamma = (N_{CEs} - N_{AEs})/N_{AEs}$) in drifter records between CEs and AEs, calculated within one quarter eddy radius from eddy center. The resulting γ rises with the Ekman pumping and saturates around 0.7 (Fig. 3m). Regional assessments confirm this increasing trend, showing steeper slopes in western boundary currents and tropical oceans (Fig. S3). This observational analysis supports that the eddy clustering asymmetry is primarily driven by Ekman pumping during eddy-wind interactions.

3.3. Principal dynamic mechanism

To further examine the role of eddy-wind interactions in driving the eddy clustering asymmetry, we conduct two numerical experiments in a rectangular domain. Model setup details are provided in the Methods section. The two experiments differ only in wind stress forcing: Experiment 1 uses absolute wind stress, which depends solely on surface winds, while Experiment 2 uses relative wind stress, accounting for the relative motion between surface winds and ocean currents (Hughes and Wilson, 2008; Zhai et al., 2012; Wilson, 2016). Therefore, relative wind stress-induced Ekman pumping is present in Experiment 2 but absent in Experiment 1. Each experiment comprises an ensemble of 10 simulations, initialized with random eddy fields reconstructed from observed eddy structures (Ni et al., 2023b). To mimic surface

drifters, Lagrangian particles anchored at a depth of ~15 m are released from every other grid point at simulation onset.

We analyze ensemble-mean Lagrangian particle distributions over the simulation duration using identical eddy detection and composite methods applied to observations. In Experiment 1, particle counts and spatial patterns are nearly identical between AEs and CEs (Figs. 4a-b), resembling observed drifter fields under weak Ekman pumping conditions (Figs. 3a-b). This homogeneous particle distribution may result from the combined effect of eddy trapping due to eddy nonlinearity and absent Ekman pumping. In contrast, Experiment 2 produces clear asymmetry: Ekman convergence drives strong particle clustering at CE cores, while Ekman divergence lowers particle concentrations within AEs (Figs. 4c-d). This pattern closely resembles the observed drifter distribution under strong Ekman pumping conditions (Figs. 3k-l). Furthermore, particle concentrations stay nearly steady in both eddy types in Experiment 1, whereas Experiment 2 shows rising (falling) concentrations inside CEs (AEs) over time (Fig. S4). The experiment comparison thus confirms eddy-wind interactions as the source of the eddy trapping asymmetry. Since eddy-induced Ekman pumping varies approximately linearly with wind speed (McGillicuddy, 2007), we run additional relative-wind-stress experiments with wind speeds ranging 2.5-22.5 m s^{-1} at 2.5 m s^{-1} intervals. Near-core $\gamma = (N_{CEs} - N_{AEs})/N_{AEs}$ also increases with wind speed and saturates near 0.9 (Fig. 4e), consistent with the observations (Fig. 3m). These simulations further support Ekman pumping as the dominant driver of the observed asymmetry.

To test the effect of β on the asymmetric particle aggregation within eddies, we repeat the numerical experiments on a β-plane with $\beta = 2\times10^{-11}$ m^{-1} s^{-1}. The clustering asymmetry pattern from the β-plane runs (Fig. S5) is qualitatively similar to the f-plane results (Figs. 4a-d). Real background winds over eddies are seldom spatially uniform (Zavala Sansón et al., 2025). We thus rerun the relative-wind-stress experiments with constant background wind stress curl, where eastward winds increase linearly from 10 m s^{-1} at the southern domain boundary to 16 m s^{-1} at the northern domain boundary. These outputs (Figs. S6a-b) agree well with the original ones forced by spatially uniform winds (Figs. 4c-d), confirming that non-uniform wind stress contributes little to the eddy clustering asymmetry. Note that, under this constant wind stress curl, the second term of Equation 2 integrated over the eddy area remains negative

for both eddy types, albeit with small magnitude (Zavala Sansón et al., 2023).

4. Conclusions

Using two decades of state-of-the-art satellite altimeter and surface drifter observations, we have presented the first comprehensive global evidence of a significant asymmetry in the aggregation of surface particles between CEs and AEs in the ocean. CEs are found to capture 12.5% more surface drifters than their anticyclonic counterparts across the global ocean, with this disparity being most pronounced at the eddy centers. Both our observational analysis and numerical model experiments demonstrate that this asymmetry results from eddy-wind interactions. Specifically, relative wind stress induces anomalous Ekman convergence in CEs and divergence in AEs, amplifying particle aggregation in CEs.

Other dynamical mechanisms may modulate particle distributions within mesoscale eddies. Submesoscale fronts have been suggested to cluster particles inside CEs (Vic et al., 2022). Yet, absolute-wind-stress experiments with 1-km resolution (submesoscale-permitting; Figs. S6c-d) closely reproduce 10-km resolution outputs (Figs. 4a-b), indicating that submesoscales are secondary for the observed asymmetry. Eddy pumping drives downwelling for growing AEs and decaying CEs and upwelling for decaying AEs and growing CEs (McGillicuddy, 2016); these competing signals cancel in composite analysis. Vortex Rossby waves induce spiral alternating upwelling and downwelling (Luo et al., 2026), which also offset in composite averages. Several mechanisms predict the opposite pattern: CEs repel near-inertial waves while AEs trap them (Kunze, 1985); barotropic anticyclones concentrate heavy particles in cyclonically rotating frame (Provenzale, 1999); the Maxey-Riley framework predicts CEs-driven dispersion and AEs-driven aggregation for inertial particles (Beron-Vera et al., 2019); bottom Ekman effect generates outward flow in CEs and inward flow in AEs (Ocampo et al., 2024).

Previous studies have shown that Ekman pumping can penetrate below the Ekman layer and decay with depth (e.g., Wilder et al., 2022; Ni et al., 2023b), implying the eddy trapping asymmetry may extend downward. However, subsurface observations resolving its vertical structure remain scarce. We apply the surface drifter analytical framework to 1000-m Argo float data. Float distributions are nearly identical inside CEs and AEs at this depth (Figs. S6e-f), indicating that the Ekman pumping-induced eddy

trapping asymmetry vanishes in the deep ocean. This places a lower bound on the vertical extent of the asymmetry. Our idealized simulations lack fully equilibrated eddy dynamics and omit real-ocean complexities, including eddy-wave interactions, variable forcing and topographic effects. Future work needs to employ more realistic simulations to further constrain this eddy trapping asymmetry.

Mesoscale eddies are ubiquitous and energetic features of the global ocean circulation, playing a key role in the transport and mixing of oceanic materials (Chelton et al., 2011; Zhang et al., 2014; Abernathey and Haller, 2018). The findings of this study provide important new insights into how mesoscale eddies redistribute surface buoyant materials in the ocean, including oil spills, plastics and phytoplankton. For instance, Ekman convergence within CEs elevates surface chlorophyll concentrations via eddy clustering, while Ekman divergence within AEs fosters phytoplankton blooms by facilitating nutrient upwelling. This asymmetry between CEs and AEs needs to be properly incorporated into the next generation of eddy parameterization schemes used for long-range climate predictions.

Acknowledgments

We thank the three anonymous reviewers for their constructive comments. Q.N. thanks Tongya Liu, Zhibin Yang, and Yafei Nie for their assistance with running the MITgcm, and Chuanyin Wang for his helpful discussion. Q.N. is supported by the National Natural Science Foundation of China (42576009) and the Southern Marine Science and Engineering Guangdong Laboratory (Zhuhai) (SML2023SP207). D.C. is supported by the National Natural Science Foundation of China (42227901).

Conflict of Interest

The authors declare no competing interests.

Open Research

All the data used in this study are publicly available. The satellite altimeter data are available at https://data.marine.copernicus.eu/product/SEALEVEL_GLO_PHY_L4_MY_008_047/description (E.U. Copernicus Marine Service Information, 2023). The drifter trajectory data are available at

http://www.aoml.noaa.gov/phod/gdp/interpolated/data/all.php (Lumpkin and Centurioni, 2019). The MERRA-2 wind data are available at https://disc.gsfc.nasa.gov/datasets/M2I1NXINT_5.12.4/summary. The ERA5 wind data are available at https://cds.climate.copernicus.eu/datasets/reanalysis-era5-pressure-levels (Hersbach et al., 2023). The Argo float data are available at https://www.argo.org.cn/index.php?m=content&c=index&a=lists&catid=101.

References

Abernathey R. & Haller, G. Transport by Lagrangian Vortices in the Eastern Pacific. J. Phys. Oceanogr. 48, 667-685 (2018).

Beron-Vera, F. J., Olascoaga, M. J., & Miron, P. Building a Maxey-Riley framework for surface ocean inertial particle dynamics. Phys. Fluids, 31(9), 096602 (2019).

Brannigan, L., Marshall, D. P., Naveira-Garabato, A. & George Nurser A. J. The seasonal cycle of submesoscale flows. Ocean Model. 92, 69-84 (2015).

Capet, X., McWilliams, J. C., Molemaker, M. J. & Shchepetkin, A. F. Mesoscale to submesoscale transition in the California Current System. Part I: Flow structure, eddy flux, and observational tests. J. Phys. Oceanogr. 38, 2256-2269 (2008).

Chaigneau, A., Texier, M. L., Eldin, G., Grados, C. & Pizarro, O. Vertical structure of mesoscale eddies in the eastern South Pacific Ocean: A composite analysis from altimetry and Argo profiling floats. J. Geophys. Res. 116, C11025 (2011).

Chelton, D. B., Schlax, M. G. & Samelson, R. M. Global observations of nonlinear mesoscale eddies. Prog. Oceanogr. 91, 167-216 (2011).

Chelton, D. B., Schlax, M. G., Samelson, R. M. & De Szoeke, R. A. Global observations of large oceanic eddies. Geophys. Res. Lett. 34, L15606 (2007).

Gruber, N., et al. Eddy-induced reduction of biological production in eastern boundary upwelling systems. Nat. Geosci. 4, 787-792 (2011).

Dong, C., Mcwilliams, J. C., Liu, Y. & Chen, D. Global heat and salt transports by eddy movement. Nat. Commun. 5, 3294 (2014).

E.U. Copernicus Marine Service Information (CMEMS). Global ocean gridded L4 sea surface heights and derived variables reprocessed 1993 ongoing. [Dataset]. Marine Data Store (MDS). https://doi.org/10.48670/moi-00148 (2023).

Ferrari, R. & Wunsch, C. Ocean Circulation Kinetic Energy: Reservoirs, Sources, and Sinks. Annu. Rev. Fluid Mech. 41, 253-282 (2009).

Frenger, I., Gruber, N., Knutti, R. & Münnich, M. Imprint of Southern Ocean eddies on winds, clouds and rainfall. Nat. Geosci. 6, 608-612 (2013).

Gaube, P., Chelton, D. B., Samelson, R. M., Schlax, M. G. & O'Neill, L. W. Satellite observations of mesoscale eddy-induced Ekman pumping. J. Phys. Oceanogr. 45, 104-132 (2015).

Gill, A. E., Green, J. S. A. & Simmons, A. J. Energy partition in the large-scale ocean circulation and the production of mid-ocean eddies. Deep-Sea Res. 21, 499-528 (1974).

Hersbach, H., et al. ERA5 hourly data on pressure levels from 1940 to present. Copernicus Climate Change Service (C3S) Climate Data Store (CDS). https://doi.org/10.24381/cds.bd0915c6 (2023).

Hughes, C. W. & Wilson, C. Wind work on the geostrophic ocean circulation, including effects of small scales in the wind stress. J. Geophys. Res. 113, C02016 (2008).

Jing, Z., et al. Maintenance of Mid-latitude Oceanic Fronts by Mesoscale Eddies. Sci. Adv. 6, eaba7880 (2020).

Kunze, E. Near-inertial wave propagation in geostrophic shear. J. Phys. Oceanogr. 15, 544-565 (1985).

Large, W. G., McWilliams, J. C. & Doney, S. C. Oceanic vertical mixing: A review and a model with a nonlocal boundary layer parameterization. Rev. Geophys. 32, 363-403 (1994).

Liu, T., He, Y., Zhai, X. & Liu, X. Diagnostics of coherent eddy transport in the South China Sea based on satellite observations. Remote Sens. 14, 1690 (2022).

Lumpkin, R. & Centurioni, L. Global Drifter Program quality-controlled 6-hour interpolated data from ocean surface drifting buoys. [Dataset]. NOAA National Centers for Environmental Information. https://doi.org/10.25921/7ntx-z961 (2019).

Luo, Q., Zhang, Z., Li, H., Wang, G., Han, G. & Li, W. High- and low-concentration spiral chlorophyll bands excited by vortex Rossby Waves. Geophys. Res. Lett. 53, e2026GL124854 (2026).

Marshall, J., Adcroft, A., Hill, C., Perelman, L. & Heisey, C. A finite-volume, incompressible Navier-Stokes model for studies of the ocean on parallel computers. J. Geophys. Res. 102, 5753-5766 (1997).

McGillicuddy, D. J. Mechanisms of physical-biological-biogeochemical interaction at the oceanic mesoscale. Annu. Rev. Mar. Sci. 8, 125-159 (2016).

McGillicuddy, D. J., et al. Eddy/wind interactions stimulate extraordinary mid-ocean plankton blooms. Science 316, 1021-1026 (2007).

McWilliams, J. C. The nature and consequences of oceanic eddies. Ocean modeling in an eddying regime 177, 5-15 (2008).

Ni, Q., Zhai, X., Jiang, X., & Chen, D. Abundant cold anticyclonic eddies and warm cyclonic eddies in the global ocean. J. Phys. Oceanogr. 51, 2793-2806 (2021).

Ni, Q., Zhai, X., LaCasce, J. H., Chen, D. & Marshall, D. P. Full-Depth Eddy Kinetic Energy in the Global Ocean Estimated from Altimeter and Argo Observations. Geophys. Res. Lett. 50, e2023GL103114 (2023a).

Ni, Q., Zhai, X., Wang, G. & Marshall, D. P. Random movement of mesoscale eddies in the global ocean. J. Phys. Oceanogr. 50, 2341-2357 (2020).

Ni, Q., Zhai, X., Yang, Z. & Chen, D. Generation of cold anticyclonic eddies and warm cyclonic eddies in the Tropical oceans. J. Phys. Oceanogr. 53, 1485-1498 (2023b).

Ocampo Jaimes, J., Zavala Sansón, L., & Graef, F. Horizontal and vertical Lagrangian dispersion in decaying cyclonic and anticyclonic vortices with lateral and bottom friction. Phys. Fluids, 36(7), 076615 (2024).

Price, J. F., Weller, R. A., & Schudlich, R. R. Wind-driven ocean currents and Ekman transport. Science 238, 1534-1538 (2008).

Provenzale, A. Transport by coherent barotropic vortices. Ann. Rev. Fluid Mech., 31(1), 55-93 (1999).

Qiu, B., & Chen, S. Variability of the Kuroshio Extension jet, recirculation gyre and mesoscale eddies on decadal time scales. J. Phys. Oceanogr. 35, 2090-2103 (2005).

Siegel, D. A., Peterson, P., McGillicuddy, D. J., Martitorena, S. & Nelson, N. B. Bio-optical footprints created by mesoscale eddies in the Sargasso Sea. Geophys. Res. Lett. 38, L13608 (2011).

Stern, M. Interaction of a uniform wind stress with a geostrophic vortex. Deep-Sea Res. 12, 355-367 (1965).

Sun, B., Liu, C. & Wang F. Global meridional eddy heat transport inferred from Argo and altimetry observations. Sci. Rep. 9, 1345 (2019).

Vic, C., Hascoet, S., Gula, J., Huck, T. & Maes, C. Oceanic mesoscale cyclones cluster surface Lagrangian material. Geophys. Res. Lett. 49, e2021GL097488 (2022).

Wilder, T., Zhai, X., Mundy, D. & Joshi, M. The response of a baroclinic anticyclonic eddy to relative wind stress forcing. J. Phys. Oceanogr. 52(9), 2129-2142 (2022).

Wilson, C. Does the wind systematically energize or damp ocean eddies? Geophys. Res. Lett. 43, 12538-12542 (2016).

Xia, Q., Li, G. & Dong, C. Global oceanic mass transport by coherent eddies. J. Phys. Oceanogr. 52, 1111-1132 (2022).

Zavala Sansó L., García-Martínez, I. M. & Sheinbaum, J. Nonlinear surface Ekman effects on cyclonic and anticyclonic vortices. J. Fluid Mech. 971, A35 (2023).

Zavala Sansón, L., García-Martínez, I. M. & Sheinbaum, J. Power input generated by a linear wind field on circular and elliptical ocean vortices. J. Phys. Oceanogr. 55(9), 1493-1506 (2025).

Zhai, X. & Marshall, D. P. Vertical eddy energy fluxes in the North Atlantic subtropical and subpolar gyres. J. Phys. Oceanogr. 43, 95-103 (2013).

Zhai, X., Johnson, H. L., Marshall, D. P. & Wunsch, C. On the wind power input to the ocean general circulation. J. Phys. Oceanogr. 42, 1357-1365 (2012).

Zhang, Z., & Qiu, B. Evolution of submesoscale ageostrophic motions through the life cycle of oceanic mesoscale eddies. Geophys. Res. Lett. 45, 11847-11855 (2018).

Zhang, Z., Wang, W. & Qiu, B. Oceanic mass transport by mesoscale eddies. Science 345, 322-324 (2014).

Figures

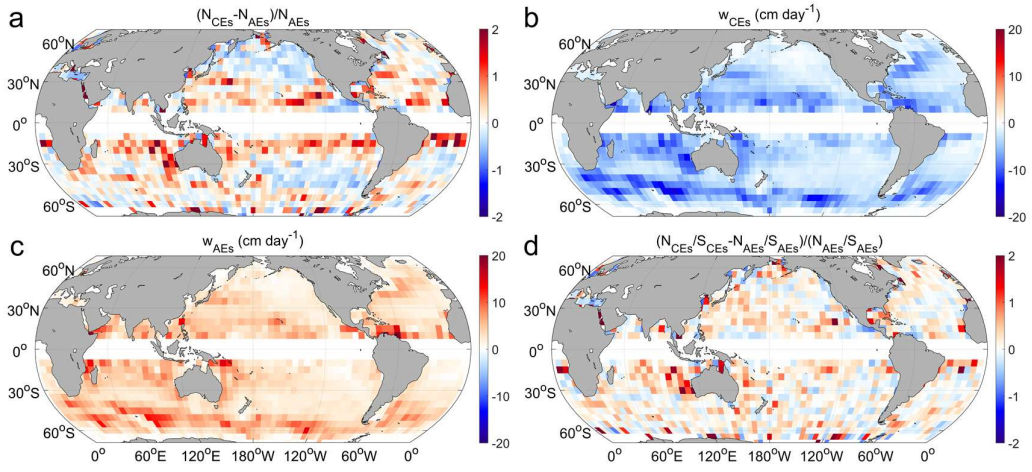
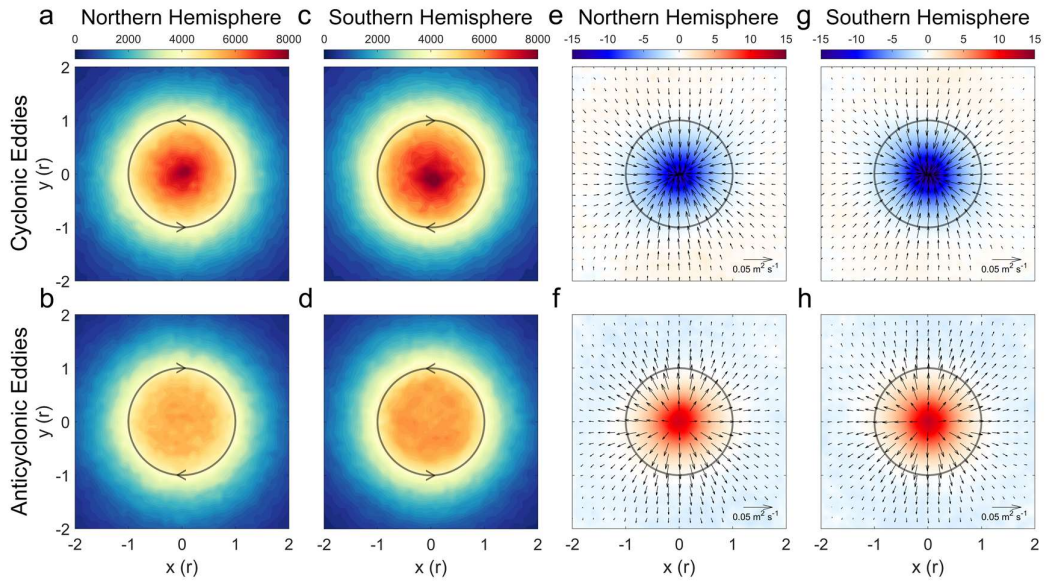


Figure 1. (a) Relative difference in drifter records within 5°×5° bins of the global ocean, computed as $\gamma = (N_{CEs} - N_{AEs})/N_{AEs}$, where N_{CEs} and N_{AEs} denote the number of drifter records inside CEs and AEs, respectively. (b) 20-year mean of Ekman pumping (cm day^{-1}) within CEs across the global ocean. (c) As Fig. 1b but for Ekman pumping within AEs. (d) As Fig. 1a but calculated using $\gamma_s = (N_{CEs}/S_{CEs} - N_{AEs}/S_{AEs})/(N_{AEs}/S_{AEs})$, where S_{CEs} and S_{AEs} denote the total area occupied by CEs and AEs within each bin, respectively.



456

457 **Figure 2.** (a, b) Numbers of surface drifter records within 0.1r×0.1r bins of an eddy-
458 centric coordinate system for cyclonic (CEs) and anticyclonic eddies (AEs) identified
459 in the Northern Hemisphere during the 20-year period from 1998 to 2017. Black circles
460 indicate the normalized edges of the eddies, and arrows indicate their rotation
461 directions. (c, d) As Figs. 2a, b but for the Southern Hemisphere. (e, f) Anomalous
462 Ekman transport (arrows; $m^2 s^{-1}$) and Ekman pumping (colour shading; cm day^{-1}) inside
463 and around CEs and AEs in the Northern Hemisphere. Ekman transport vectors and
464 Ekman pumping velocities are calculated from global daily MERRA-2 winds and
465 altimeter-derived geostrophic currents and then interpolated to the locations of surface
466 drifters. (g, h) As Figs. 2e, f but for the Southern Hemisphere.

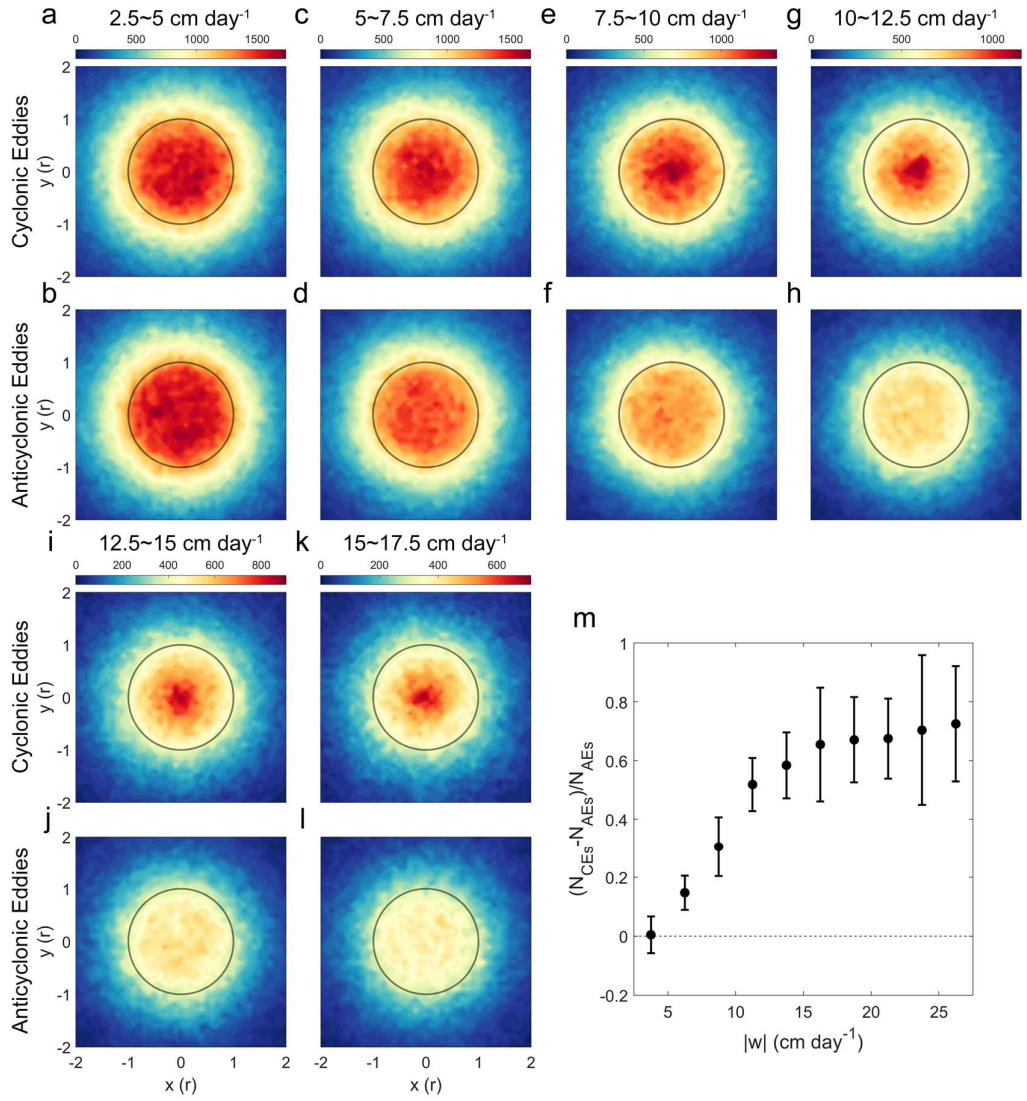
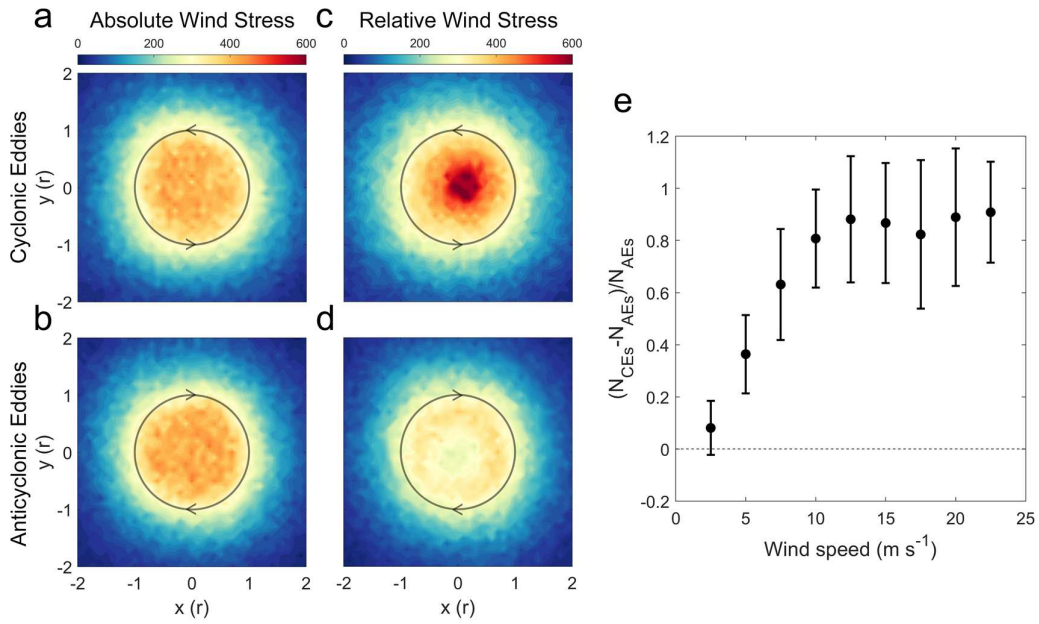


Figure 3. (a-l) Numbers of surface drifter records associated with CEs and AEs, grouped by the magnitude of relative wind stress-induced Ekman pumping velocity (cm day^{-1}). (m) Relative difference in drifter record numbers between the two types of eddies (averaged within one quarter of the eddy radius from the eddy center) plotted as a function of the magnitude of Ekman pumping velocity. Vertical bars represent one standard deviation.



474

475 **Figure 4.** Numbers of Lagrangian particles within and around (a) CEs and (b) AEs in
476 Experiment 1 forced by absolute wind stress. (c, d) As Figs. 4a, b but for Experiment 2
477 forced by relative wind stress. (e) Relative difference in Lagrangian particle numbers
478 between the two types of eddies (averaged within one quarter of the eddy radius from
479 the eddy center) plotted as a function of the magnitude of wind speed used in relative-
480 wind-stress experiments. Vertical bars represent one standard deviation.